Article

High-capacity water sorbent cycles without hysteresis under dry conditions

Julius Oppenheim [1,3], Zhentao Yang[1,3], Bhavish Dinakar[2] & Mircea Dincă [1,2] ✉

Sorbents capable of cycling water vapor under dry conditions are critical for applications such as atmospheric water harvesting, desiccation, and heat pumps; however, few existing sorbents demonstrate both hysteresis-free behavior and cycling stability. Here we show that post-synthetic exchange with lithium, sodium, potassium, magnesium, and tetramethylammonium in the metal-organic framework (MOF) SU-102 ($[(CH_3)_2NH_2]_2[Zr(HL)_2]$; H_4L = ellagic acid) enables high-capacity water sorption under low humidity ranging from 11.1% to 4.3%. The champion material, Mg-SU-102, exhibits sharp water uptake at 4.3% RH, reaches a high maximum gravimetric capacity of 0.41 g/g (with 0.29 g/g at 15% RH), and displays minimal capacity loss over 500 adsorption-desorption cycles, with essentially no hysteresis. We use vibrational Stark spectroscopy to probe the local electric field environment within each ion-exchanged material and show that the trend in relative humidity follows a Hofmeister-type series in which the cation affects the ability for water to solvate the framework pores. We find strong deviation from this trend for the tetramethylammonium material, as the larger cation does not undergo capillary condensation sorption, suggesting that fine control over pore functionality is necessary. Establishing a correlation between water sorption and a Hofmeister-type series provides foundational principles for the design of porous ionic sorbents.

Sorbents that can cycle large quantities of water at low relative humidity (RH) with minimal hysteresis (to promote fast cycling and energy efficiency) are critical for atmospheric water harvesting in arid regions, desiccation, and heat pumps[1–4]. However, there have been only a few sufficiently hydrophilic sorbents that exhibit high water uptake capacity (>0.3 g/g) at low RH (<15%)[5]. There are even fewer sorbents that achieve these criteria with small adsorption-desorption hysteresis and good cycling stability, as highly hydrophilic materials must withstand the demanding conditions required for water release. Recent literature has proposed that the most effective approach to achieve high-capacity sorption at low RH involves invoking an isoreticular modification to increase the hydrophilicity of a high-capacity sorbent (rather than the alternative of isoreticular contraction, which

decreases capacity)[6]. The apparent absence of sorbents that match all the criteria may, in part, result from a conflict in which sorbents must be sufficiently hydrophilic to have step-wise sorption at low RH, but not too hydrophilic to prevent the onset of kinetic hysteresis.

Metal-organic frameworks (MOFs) have been proposed as useful water sorbents as constituent modularity enables rational modification for tuning the capacity and uptake RH. Isoreticular modifications of the ligand composition[7–12], metal node identity[6,13–17], bridging and terminal anion identity[6,18] have been studied as means to vary the hydrophilicity of the framework. However, there have only been limited investigations into the effect of variation of charge-balancing cations located within the pores on water sorption, and no systematic trends have been reported in this sense[19]. Because the guest/charge-

[1]Department of Chemistry, Massachusetts Institute of Technology, 77 Massachusetts Avenue, Cambridge, Massachusetts, USA. [2]Department of Chemical Engineering, Massachusetts Institute of Technology, 77 Massachusetts Avenue, Cambridge, Massachusetts, USA. [3]These authors contributed equally: Julius Oppenheim, Zhentao Yang. ✉e-mail: mdinca@mit.edu

balancing ions are much more likely to interact strongly with guest water molecules than the hydrophobic organic ligands or the mostly coordinatively saturated metal nodes studied previously, they could have a larger impact on overall water sorption. Indeed, we surmised that even small changes to the identity of pore-dwelling cations can impart large changes especially on the RH for the onset of water sorption.

Herein, we establish the effects of pore cation identity on the RH adsorption step for the anionic MOF SU-102 ($M_xZr(HL)_2$; H_4L = ellagic acid, M = dimethylammonium [DMA], lithium, sodium, potassium, tetramethylammonium [TMA] ($x = 2$), magnesium ($x = 1$)) (Fig. 1)[20]. SU-102 was chosen as a representative framework, having been previously demonstrated to be water stable and susceptible to cation exchange. We find that sorption follows a Hofmeister-type series[21,22], wherein Mg^{2+} (a strong kosmotrope) shifts the adsorption step to the lowest RH. We quantify this series via vibrational Stark spectroscopy, using the $\nu_{asym}(C=O)$ mode of the ellagic acid linker as a Stark probe, and find a correlation ($R^2 = 0.99$) between the $\nu_{asym}(C=O)$ frequency and the critical RH following: $RH = e^{0.081\nu(C=O)-139.66}$. Though the Hofmeister-type series is qualitatively suitable, it falls short on the absolute RH trend by predicting K <Na <Li, rather than K <Li <Na. Additionally, the series is not sufficient to predict that TMA-SU-102 adsorbs by a non-stepwise sorption (capillary condensation) mechanism. Other factors, such as the size of the cation and its primary coordination sphere (modulating the effective pore size), also shift the adsorption step position and affect the sorption mechanism. We find that Mg-SU-102 displays unprecedented high capacity at low RH, with an onset for adsorption at 4.3% RH and a capacity of 0.29 g/g at 15% RH. Likewise, Mg-SU-102 displays minimal sorption hysteresis and displays little degradation over at least 500 adsorption-desorption cycles.

Results and Discussion
Synthesis and structure
M-SU-102 (M = DMA, Li, Na, K) were synthesized from ellagic acid using a protocol adapted from literature[20]. These isoreticular frameworks crystallize as hexagonal nets, comprised of chains of square antiprismatic Zr (each connected to 4 catecholates) bridged by stacks of canted ellagic acid. The pore limiting diameter for the hexagonal pores

is 11.5 Å, which is, in part, occupied by pore cations. Mg-SU-102 and TMA-SU-102 were synthesized by analogous exchange using either $MgCl_2$ or TMACl as a cation source. Inductively coupled plasma-mass spectrometry (for Li, Na, K, and Mg) and NMR spectroscopy (for TMA) of the respective digested frameworks confirmed near stoichiometric exchange for each of the cations after two one-day soaking cycles at room temperature (Li 99.75%, Na 98.25%, K 98.95%, Mg 95.7%, TMA ~100%).

All exchanged materials display similar crystallinity and porosity as measured by powder X-ray diffraction (PXRD) and N_2 sorption analysis (Fig. 2, Table 1), with apparent BET surface areas in line with literature values. The N_2 BET surface area of DMA-SU-102 is 605 m^2/g, Li-SU-102 is 722 m^2/g, Na-SU-102 is 601 m^2/g, K-SU-102 is 475 m^2/g, Mg-SU-102 is 505 m^2/g, and TMA-SU-102 is 340 m^2/g. The N_2 pore volume for DMA-SU-102 is 0.30 cm^3/g, Li-SU-102 is 0.50 cm^3/g, Na-SU-102 is 0.31 cm^3/g, K-SU-102 is 0.35 cm^3/g, Mg-SU-102 is 0.25 cm^3/g, and TMA-SU-102 is 0.22 cm^3/g, in accordance with literature values (Table 1). Minor differences among surface areas and pore volumes can be attributed to the different masses of the cations as well as their primary coordination sphere of water. The coordinated water is not removed upon activation at 80 °C, as revealed by thermogravimetric analysis, which shows minimal mass loss between 80 °C up to the point of material degradation.

Water adsorption measurements
Water sorption isotherms measured at 25 °C for DMA-, Li-, Na-, K-, and Mg-SU-102 exhibit sigmoidal behavior, consistent with a capillary condensation mechanism with an initial pre-wetting sorption event (at either the Zr nodes or on the metal cations)[23,24]. The critical RH (defined by the inflection point) follows the trend Mg <K <Li <Na <DMA (Table 1). The maximum gravimetric capacity follows the expectation given the mass of as well as volume occupied by each ion and their respective solvation shell per charge, following Mg > Li > Na > K > DMA. Each material also displays no significant loss in crystallinity after water sorption (Figures S1–S6).

Each of the isotherms were fit to an empirical functional form that describes the low-pressure and high-pressure regimes as Langmuir-Freundlich curves joined together by a logistic (sigmoid) function, with an additional logistic function used to describe interparticle condensation near 100% RH (Supplemental Section 4). The RH of the step function was taken as the position of the logistic function, which lies between 4.3% and 11.1% RH. Remarkably, even though the materials display stepwise isotherms, there is no significant amount of adsorption-desorption hysteresis (Figures S8–S13). This absence may be attributed to the pore size, at 11.5 Å diameter, being less than the critical diameter of 20 Å.[1]

Curiously, a mechanism involving capillary condensation is not conserved for every cation type. Indeed, TMA-SU-102 exhibits similar porosity and crystallinity to the other frameworks, but does not display stepwise sorption (Fig. 3). Instead, the framework exhibits Type I isotherm behavior in the low-pressure region, with a slight uptick in sorption at the highest RH. The initial rise in loading occurs at approximately 3.5% RH (estimated by the RH at half-capacity near the plateau at 60% RH). There are two potential explanations for the loss of capillary condensation. First, a shift to lower RH and loss of capillary condensation is consistent with a decrease in the effective pore size[6]. Second, TMA cations may impede the formation of the hydrogen bonding network as they cannot participate in hydrogen bonding.

Variable temperature water isotherms between 15 °C and 55 °C were measured for the best performing material, Mg-SU-102 (Fig. 4). Each of the isotherms displays similar sigmoidal behavior with a step between 2% and 6% RH. The characteristic curves (calculated as $A = RT \ln[P_O/P]$, where R is the ideal gas constant, T is temperature, P_O is the saturation vapor pressure, and P is the vapor pressure) overlap well, with a slight shift towards lower energies at higher temperatures. This
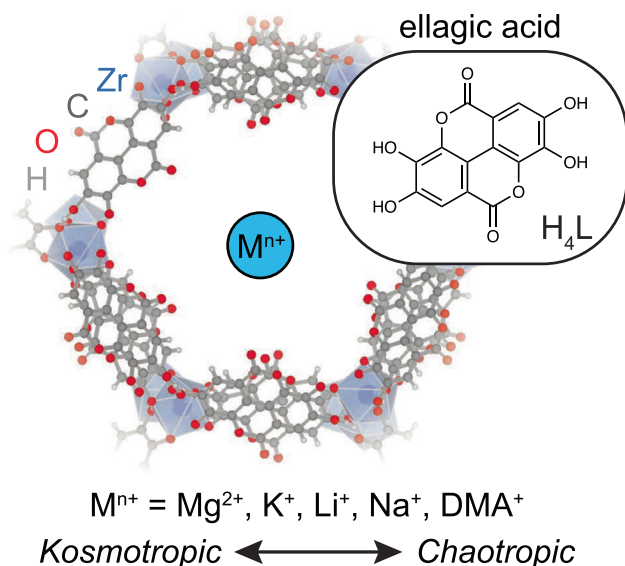

Fig. 1 | Structure of M-SU-102. Structure of M-SU-102 (CCDC: 2167934; M-SU-102 = [Zr(HL)$_2$]; H$_4$L ellagic acid and M dimethylammonium [DMA], lithium [Li], sodium [Na], potassium [K], magnesium [Mg], or tetramethylammonium [TMA];) viewed down the c-axis. Scale of the cations from kosmotropic (causing ordering) to chaotropic (causing disordering).
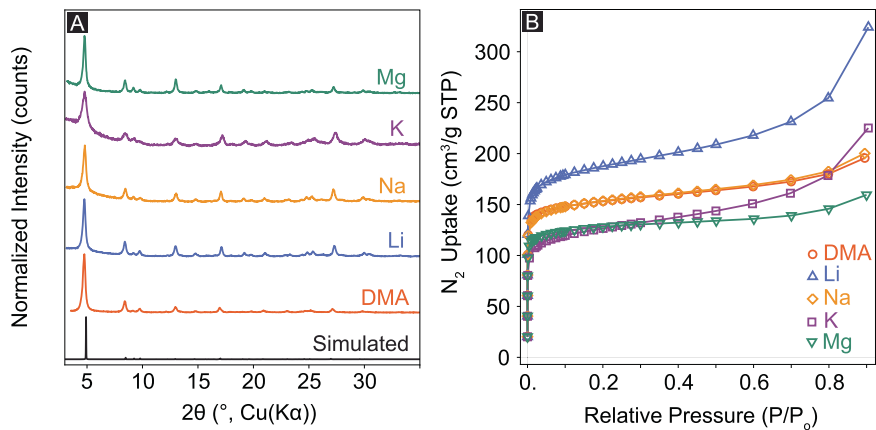
$M^{n+} = Mg^{2+}, K^+, Li^+, Na^+, DMA^+$

Kosmotropic ⟵ ⟶ *Chaotropic*

Fig. 2 | Characterization of M-SU-102 crystallinity and porosity. A Powder X-ray diffraction patterns. **B** 77 K N_2 sorption isotherms for M-SU-102 (M = DMA, Li, Na, K, Mg).

Table 1 | List of MOFs: relative humidity (taken as the RH of the step from the best fit), capacity, $v_{asym}(C = O)$ in the pore filled state, N_2 surface area

Framework	Relative humidity (%)	Maximum gravimetric capacity H_2O (g/g)	Capacity at 15% RH (g/g)	$v_{asym}(C = O)$ humid state (cm^{-1})	N_2 surface area (m²/g)	N_2 pore volume (cm³/g)
DMA-SU-102	11.1	0.28	0.15	1701	605	0.30
Li-SU-102	7.8	0.40	0.25	1698	722	0.50
Na-SU-102	8.5	0.37	0.22	1697	601	0.31
K-SU-102	6.3	0.49	0.20	1696	475	0.35
Mg-SU-102	4.3	0.41	0.29	1687	505	0.25
TMA-SU-102	3.5*	0.25	0.14	1695	340	0.22

Capacity at 15% RH calculated using best fit model. *RH is estimated by the RH at half-capacity compared to 60% RH, as there is no sorption step.
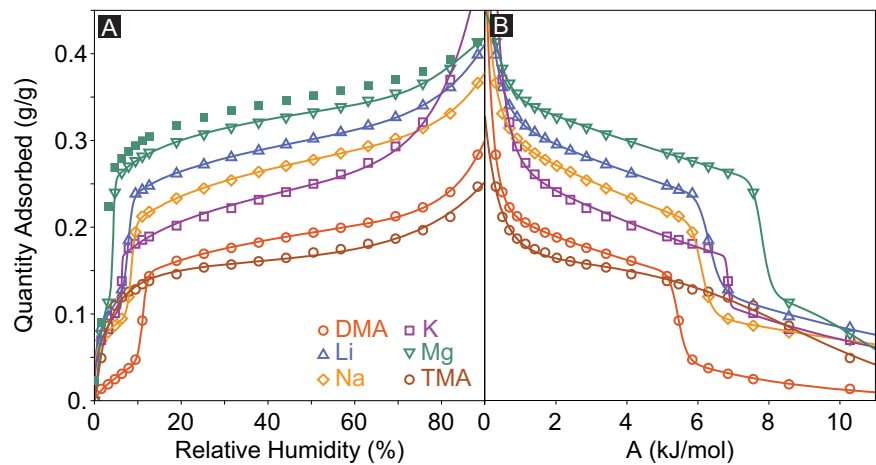

Fig. 3 | Water sorption properties of M-SU-102. A Water sorption isotherms at 25 °C (the filled green square depicts a representative desorption isotherm for Mg-SU-102); (**B**) characteristic curves with best fit models for M-SU-102 (M = DMA, Li, Na, K, Mg, TMA).

slight change, concomitant with the increase in RH of the step, is attributed to entropic contributions from capillary condensation[25]. There is no significant increase in the size of the hysteretic loops at low temperatures (Figure S18) nor decrease in the slope of the sorption step at high temperatures, consistent with no sorption critical temperatures (either hysteresis or pore critical temperatures) in the 15 °C to 55 °C range.

The isosteric enthalpy for water sorption was calculated in the 25 to 40 °C range, as only the isotherms within this temperature range have sufficient data points for reliable fits in each regime on either side of the critical RH. The isosteric enthalpy was calculated to be −49 to −56 kJ/mol in the step, only slightly higher than the enthalpy of vaporization of pure water[26].

To assess the potential usability of the best performing Mg-SU-102, we measured 512 pressure swing adsorption-desorption cycles (PSA) (Fig. 5). The PSA was measured between 0% and 15% RH, under a constant temperature of 25 °C, with an equilibration time of 30 min for each half cycle. Under these specific conditions, adsorption kinetics are rapid, with saturation occurring in under 10 minutes, whereas desorption kinetics are more sluggish with equilibrium reached within roughly 30 min. There is a slight initial decrease in working capacity over the first 50 cycles, associated with a decrease in the mass
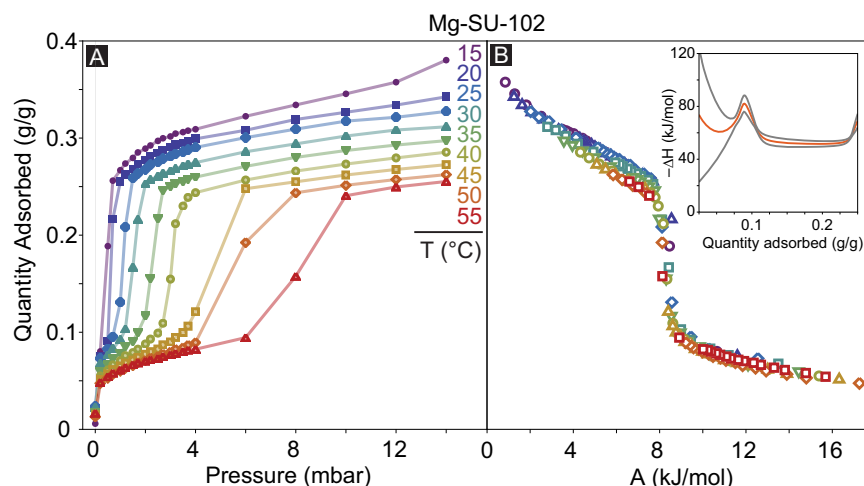
Fig. 4 | Variable temperature water sorption behavior of Mg-SU-102. A Variable temperature water isotherms (displayed with linear interpolation as a visual guide) and (**B**) characteristic curves of Mg-SU-102. (Inset) Isosteric enthalpy of adsorption (Δ*H*) calculated from the 25, 30, 35, and 40 °C isotherms.
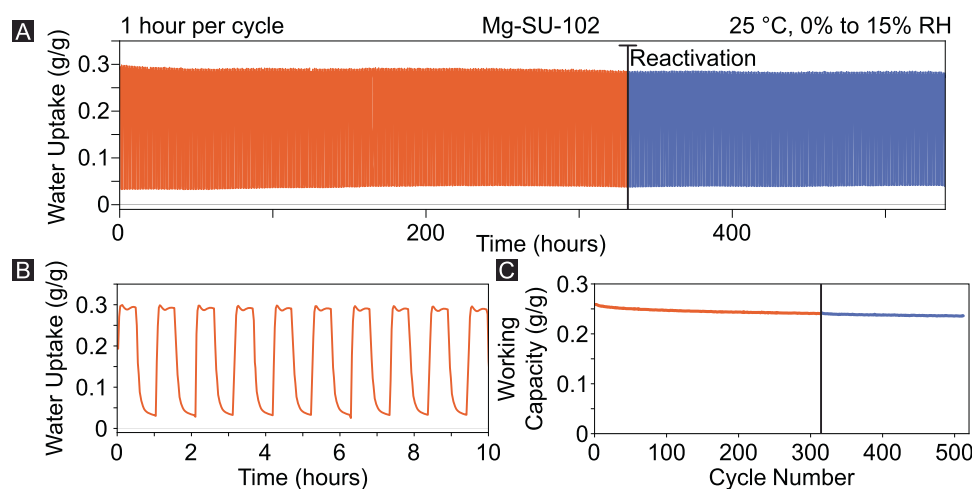

Fig. 5 | Water cycling behavior of Mg-SU-102. A Pressure swing adsorption-desorption (PSA) cycling of Mg-SU-102 between 0% and 15% RH at 25 °C. The vertical line indicates a 70 °C activation. **B** Magnified gravimetric trace for the initial 10 PSA cycles. **C** Working capacity for each cycle.

of the sample after adsorption caused by a decrease in the total capacity of the sorbent (with a constant mass after desorption) (Figures S32–S33). Afterwards, there is a near linear decrease in capacity, with a slope of about $-2.8 \cdot 10^{-5}$ (g/g)/cycle. A decrease in working capacity can often be attributed to slow kinetics leading to diminished steady state working capacity[27]. However in the case of Mg-SU-102, the initial working capacity is not recovered after reactivation after 315 cycles, suggesting that the decrease in working capacity, albeit small, is irreversible and not caused by short cycling times.

Mg-SU-102 displays good stability when compared against other hydrophilic MOFs that adsorb water below 10% RH. Whereas Mg-SU-102 has a 1% decrease in working capacity every 56 cycles (over all 512 cycles), most other frameworks lose capacity 10 times faster: ~1% in fewer than 5 cycles. This performance is notable, especially because Mg-SU-102 demonstrates one of the highest capacities for MOF sorbents that operate under extreme dryness, below 5% RH (Table 2).

Influence of local solvent structure on water sorption; mechanistic studies of water uptake
To investigate details of the water network within the pores for both activated and pore-filled states, in situ infrared spectroscopy measurements were conducted in a diffuse reflectance geometry. Samples of various frameworks were measured under two conditions: upon

activation under a flow of dry nitrogen gas, and pore-filled by a water-saturated flow of nitrogen gas passed through a fritted bubbler filled with water.

In the activated state, the Li-, Na-, K-, and Mg-SU-102 spectra each exhibit a sharp band between 3680 and 3700 cm^{-1} consistent with the presence of free water (bound to a cation, but not hydrogen-bonded to other water molecules)[28]. Conversely, the spectra of DMA-SU-102 and TMA-SU-102 do not display a free water signal (Figure S20). This suggests that in the activated state, the cations within Li-, Na-, K-, and Mg-SU-102 are each solvated by a primary coordination sphere of water, whereas the cations within DMA- and TMA-SU-102 are not.

Additionally, in the activated state, the two ν(C = O) modes for ellagic acid (symmetric and antisymmetric) decouple from each other, and two vibrational bands are observed. This is consistent with an asymmetric pore environment, where the cations coordinate closely to the linkers, as compared to the symmetric pore environment of the humid state, where water screens the cations and only the antisymmetric mode is observed. Interestingly, the ν(C = O) bands are not split in the spectrum of activated TMA-SU-102, suggesting that the TMA cation interacts only weakly with the linker ester, and does not break the centrosymmetric symmetry.

We hypothesized that the differences in cation-dependent water sorption free energies would manifest in different intraporous solvent

Table 2 | Water sorption properties for MOFs with a critical RH below 10%

Framework	Critical relative humidity (%)	Gravimetric capacity above sorption step (at 20% RH) (g/g)	Cycling stability	Reference
Mg-SU-102	4.3	0.30	9.1% decrease in capacity after 512 cycles (56 cycles/1% loss)	This work
Co$_2$Cl$_2$BBTA	2	0.37	Not reported	17
Ni$_2$Cl$_2$BBTA	3	0.34	11% decrease in working capacity after 9 cycles (0.8 cycles/1% loss)	17
CAU-6(Al)	4.5	0.27	Not reported	38
Ni$_{50}$,Zn$_{50}$-MOF-74	9	0.48	15% decrease in capacity after 9 cycles (0.6 cycles/1% loss)	13
CAU-10-pydc	9	0.35	No loss in capacity after 50 cycles	39
MIL-160	9	0.34	Minimal decrease in capacity over 10 cycles	40,41
MOF-801-P	9	0.28	3.5% decrease in capacity after 5 cycles (1.4 cycles/1% loss)	42
MOF-804(Zr)	10	0.16	27% decrease in working capacity after 4 cycles (0.1 cycles/1% loss)	42

structures in the pore-filled state, as previously observed, for instance, in zeolites upon altering hydrophilicity and pore structure[29,30]. To test this hypothesis, we employed vibrational Stark spectroscopy – an infrared technique pioneered for the characterization of local electric fields (E-fields) at enzyme active sites – as a quantitative metric for pore water structure[31]. This technique probes local E-fields that may be induced by nearby E-fields, including externally applied capacitive E-fields, charged or highly polar functional group residues[32], solvation-induced E-fields caused by solvent dipoles[33], or interfacial E-fields pertaining to electrochemical double-layers[34].

Relevantly here, frequencies of C = O stretching modes in probe molecules (denoted Stark probes) have been demonstrated to follow a robust linear correlation with local E-field through the equation $\Delta\nu_{obs} = \Delta\vec{\mu} \bullet \vec{E}$, where $\Delta\nu_{obs}$ is the frequency shift relative to zero-field (i.e., gas-phase) environment, $\Delta\vec{\mu}$ is the vibrational Stark tuning rate (in units of cm^{-1}/(MV/cm)) specific to the C = O stretch, and $\vec{E}$ is the local E-field along the C = O bond[31].

In SU-102, the carbonyl groups of ellagic acid can serve as Stark probes to quantify the local E-field exerted by a combination of adsorbed water molecule dipoles and cation charge in the pore-filled state. Unlike typical Stark probe molecules that contain a single C = O vibrational mode, the SU-102 linker contains two symmetrically equivalent lactone C = O bonds that couple to form IR-active anti-symmetric and IR-inactive symmetric stretching modes. In the presence of a uniform E-field oriented parallel to one of the C = O bonds, the Stark tuning rate is identically zero because a positive E-field along one C = O bond direction results in a negative E-field of the same magnitude along the opposite C = O bond direction. Resultantly, ν_{asym}(C = O) is not a useful reporter of the local E-field at the C = O bonds in the presence of a uniform E-field. However, in the pore-filled state, the E-field at the center of a C = O bond is not caused by a uniform E-field, but rather originates from a combination of water molecule dipoles that orient in a stabilizing response to the MOF dipoles, as well as the charge-balancing cation in the pore, which will adopt the same symmetry as the MOF. As such, the resultant E-field about the linker will be quadrupolar rather than dipolar. Critically, this means that an E-field along the C = O bond would result in an E-field of opposite direction as the other C = O bond in the same linker, contrary to the case for a uniform E-field. Hence, although the Stark tuning rate for ν_{asym}(C = O) in the presence of a uniform E-field is identically zero, the "quadrupolar Stark tuning rate" (i.e., the frequency shift in response to an E-field that is equal but opposite in direction at each C = O bond) may not be zero, allowing ν_{asym}(C = O) to serve as a useful probe of local E-field strength at the C = O bond.

Gratifyingly, density functional theory (DFT) calculations using point charges to create quadrupolar E-fields up to 50 MV/cm at the C = O bonds predict that the ellagic acid linker displays a quadrupolar Stark tuning rate similar in magnitude to dipolar Stark tuning rates expected for asymmetric model molecules such as ethyl acetate. This justifies the interpretation of a shift in ν_{asym}(C = O) as a local reporter of a quadrupolar E-field experienced by ellagic acid in the pore-filled states of SU-102 materials (Supplemental Section 8).

Experimentally, we find that contributions of the local E-field from water (in the absence of cations) account for a red shift from the gas-phase frequency of 1761 cm^{-1} (DFT calculated ellagic acid) to 1716 cm^{-1} (ellagic acid measured in aqueous solution). Further red shifts from 1716 cm^{-1} can be interpreted as the result of the cation affecting the local E-field as well as the cation restructuring the pore water network.

Upon cation exchange, a shift of the ν_{asym}(C = O) mode from 1701 cm^{-1} to 1687 cm^{-1} is observed, with the order of decreasing frequency as DMA > Li > Na > K > TMA > Mg (Fig. 6a). If the red-shift is solely attributed to changes in local E-field, and under the assumption that the vibrational Stark tuning rate is 0.61 cm^{-1}/(MV/cm) (Supplemental Section 8), then bulk water contributes 74 MV/cm, DMA$^+$ contributes an additional 25 MV/cm, and Mg^{2+} contributes an additional 48 MV/cm. The changes in local E-field are loosely correlated with the critical RH for water uptake, wherein the frameworks with the most amount of redshift exhibit the lowest RH for uptake (Fig. 6b). Specifically, the logarithm of RH is loosely linearly correlated with the local E-field. We note that because TMA-SU-102 uptakes water with a non-capillary condensation mechanism, it is not included in this correlation.

The influence of the cation on sorption can be interpreted as a Hofmeister-type series, in which the cation affects the solubility of the MOF[35]. More precisely, the cation (either directly, or indirectly, depending on how the cation solvation shell interacts with nearby waters) affects the ability of the pore to be solvated by water molecules. The relative cation ordering in this Hofmeister-type series, and the conventional description by use of Jones-Dole equation B-coefficients, both situate magnesium as the most kosmotropic cation, but differ in the ordering for the other cations[21]. The disagreement is not surprising as the ordering depends upon the identity of the solute; thus, the relationship between local E-field and framework solubility may be imperfect.

Post-synthetic cation exchange within a series of anionic MOFs has been analyzed as a means for tuning the critical RH for water sorption. We find that the charge-balancing cation plays a critical role in determining the RH for sorption. Modification from the native dimethylammonium cation in SU-102 to magnesium shifts the RH from 11.% to 4.3% RH. Vibrational Stark spectroscopy helped quantify the local electric field imposed by the various cations (and their water solvation shells), establishing a qualitative correlation with a
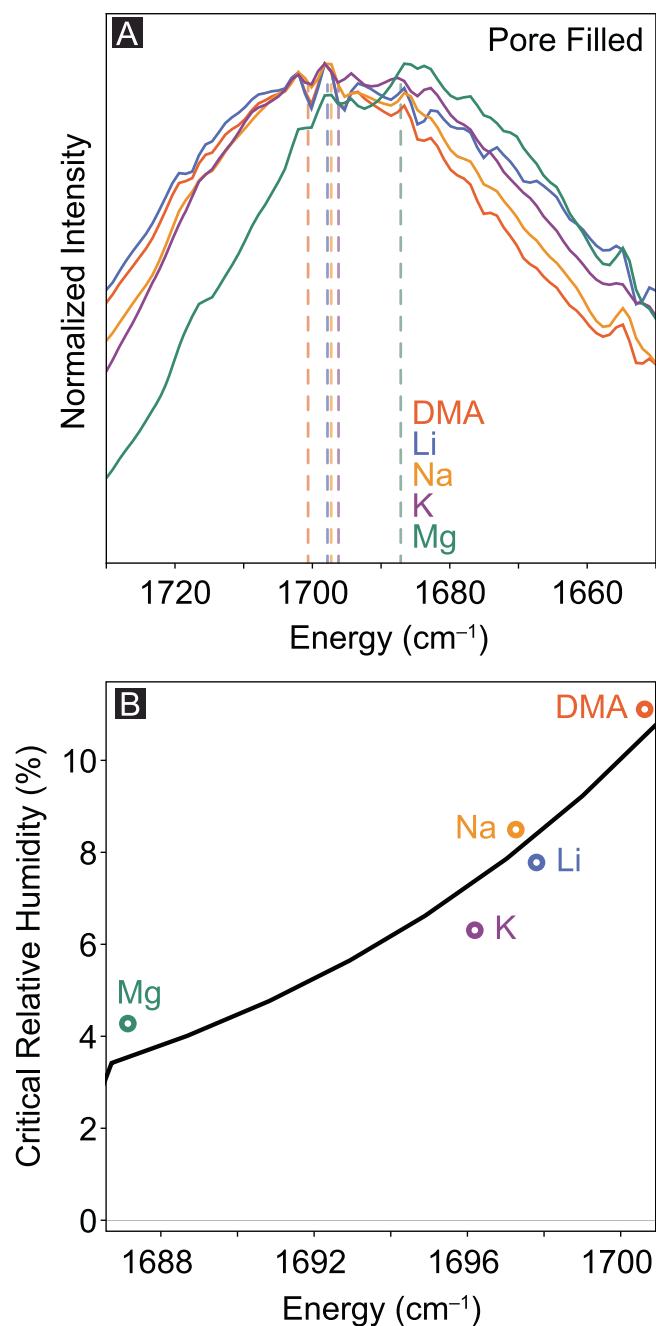
Fig. 6 | Spectroscopic characterization of M-SU-102. A $v_{asym}(C=O)$ band of pore-filled frameworks for M-SU-102 with dashed line indicating the peak maximum. **B** Correlation between the $v_{asym}(C=O)$ frequency and critical RH; the line is a fit corresponding to the function: $RH = e^{av_{C=O} + b}$ ($R^2 = 0.992$; $a = 0.08 \pm 0.02$; $b = -139.66 \pm 31.73$).

Methods

Synthesis of DMA-SU-102. The synthesis was scaled up two times from the previous report[20]. 1200 mg of ellagic acid (97%, Thermo Scientific, 2 eq.) and 640 mg of ZrOCl$_2$·8H$_2$O (99.9%, Alfa Aesar, 1 eq.) were added to a 200 mL round-bottom flask containing 40 mL N,N-dimethylformamide (DMF) (≥99.9%, VWR), 20 mL deionized water, and 30 mL glacial acetic acid (≥ 99.7%, Sigma-Aldrich). The mixture was heated at 80 °C with stirring for 48 hours in an oil bath with a reflux condenser. The solids were separated from excess DMF and acetic acid by centrifugation at 3260 g for 10 minutes. The solids (200 mg at a time) were then washed three times with 20 mL water for 1 day each, using centrifugation to separate the solids each time. The solids were dried at 80 °C under air overnight.

Exchange DMA-SU-102 to M-SU-102 (M = Li$^+$, Na$^+$, K$^+$, Mg^{2+}, TMA$^+$). 100 mL of 1 M MCl$_n$ aqueous solution (M = Li$^+$, Na$^+$, K$^+$, Mg^{2+}) (LiCl anhydrous, 98%, Alfa Aesar; NaCl anhydrous, high purity grade, VWR; KCl anhydrous, ACS reagent, Sigma-Aldrich; MgCl$_2$ anhydrous, 99%, Alfa Aesar) or 2 M (TMA)Cl (synthesis grade, Sigma-Aldrich) was added to 200 mg of DMA-SU-102 and stirred at room temperature for 1 day. The mixture was centrifuged at 3260 g for 5 minutes to separate the solids. The solvent was replaced with 100 mL of 1 M MCl aqueous solution and stirred at room temperature for 1 day. The mixture was centrifuged at 3260 g for 5 minutes to separate the solids. The solids were washed with deionized water by two one-day soaks at room temperature, using centrifugation to separate the solids.

Nitrogen adsorption isotherms were measured by a volumetric method using a Micromeritics ASAP 2020 Plus gas sorption analyzer. Typical samples of 30–60 mg were loaded into a pre-weighed analysis tube and capped with a Micromeritics TranSeal. The tube was activated at 80 °C under dynamic vacuum on the degas port of the gas sorption analyzer for 24 h and cooled to room temperature. The tube was then reweighed to determine the mass of the sample and the pre-weighed tube. Free space correction measurements were performed using ultra-high purity He gas (UHP grade 5, 99.999% pure). Nitrogen isotherms were measured using UHP grade nitrogen. All nitrogen analyses were performed using a liquid nitrogen bath at 77 K. Oil-free vacuum pumps were used to prevent contamination of samples or feed gases.

Water vapor adsorption isotherms and water cycling experiments were conducted using a gravimetric method with a Hiden Analytical XEMIS microbalance equipped with a vapor dose option and a heated manifold. A typical MOF sample weighing approximately 3–5 mg was loaded into the microbalance basket, and activated under vacuum for 8 hours with a programmable water bath with a recirculating chiller set to 70 °C. Water analyses were carried out at variable temperatures using the water bath with recirculating chiller, and oil-free vacuum pumps were utilized to avoid any sample or feed gas contamination.

Diffuse reflectance infrared Fourier transform spectroscopy (DRIFTS) were performed using a Bruker Tensor 37 IR spectrometer equipped with a liquid nitrogen-cooled mercury cadmium telluride detector and a Pike DiffusIR™ accessory. Samples were loaded under air and diluted with KBr in a ratio of about 1:25-100 (MOF:KBr). The sample was activated under a constant flow of 100 sccm nitrogen at 35 °C. Dosing was performed by a flow of nitrogen gas passed through a fritted bubbler filled with water (100 sccm). The humid IR spectra were corrected in order to remove signal originating from water vapor.

Powder X-ray Diffraction (PXRD). A Bruker Advance II diffractometer with θ/2θ reflection geometry and Ni-filtered Cu Kα radiation (Kα1 = 1.5406 Å, Kα2 = 1.5444 Å, Kα2/ Kα1 = 0.5) was used to record PXRD patterns. The tube voltage and current were set at 40 kV and 40 mA, respectively. Thin layers of the samples were placed on zero-background silicon crystal plates before PXRD measurements.

Nuclear magnetic resonance (NMR) experiments were performed on a three-channel Bruker Avance Neo spectrometer (500 MHz). ^{1}H-NMR spectra are internally referenced to residual solvent signal at

Hofmeister-type series, whereby cations that induce greater changes to the local electric field and pore water structure, increase the hydrophilicity of the framework by the greatest amount. We further show that this correlation holds for cations that allow capillary condensation, thus excluding larger/greasier ions such as tetramethylammonium. Owing to their higher charge/radius ratio and their divalent nature, which reduces the mass of charge-balancing ions by half, Mg^{2+} ions produce a particularly compelling material, Mg-SU-102. This MOF reaches a saturation gravimetric capacity of 0.41 g/g, is notably stable to pressure-swing water sorption cycling, comparing favorably on both accounts with other materials that function under extremely dry conditions (RH < 10%).

$\delta = 2.50$ (DMSO-d_6). ^{13}C-NMR spectra are internally referenced to residual solvent signal at $\delta = 39.52$ (DMSO-d_6). 3 mg DMA-SU-102 was digested in 50 μL D$_2$SO$_4$ with 5 minutes of sonication, and 600 μL of DMSO-d_6 were added to the solution. ^{1}H NMR (500 MHz, DMSO) δ 13.07 (s, H$_2$SO$_4$), 7.38 (1 s, C$_{14}$H$_2$O$_8$), 2.39 (3.17, (CH$_3$)$_2$N). ^{13}C NMR (126 MHz, DMSO) δ 159.54, 148.27, 139.64, 136.70, 112.72, 110.71, 108.19, 34.90/34.81/34.71 (t, (CH$_3$)$_2$NH$_2$).3 mg TMA-SU-102 was digested in 50 μL D$_2$SO$_4$ with 5 minutes of sonication, and 600 μL of DMSO-d_6 were added to the solution. ^{1}H NMR (500 MHz, DMSO) δ 12.85 (s, H$_2$SO$_4$), 7.42 (1 s, C$_{14}$H$_2$O$_8$), 3.03 (6.35 s, (CH$_3$)$_4$N). ^{13}C NMR (126 MHz, DMSO) δ 160.08, 148.77, 140.13, 137.20, 113.24, 111.26, 108.72, 55.20/55.17/55.14 (t, (CH$_3$)$_4$N). 3 mg M-SU-102 (M = Li, Na, K, Mg) was digested in 50 μL D$_2$SO$_4$ with 5 minutes of sonication, and 600 μL of DMSO-d_6 were added to the solution. ^{1}H NMR (500 MHz, DMSO) δ 13.18 (s, H$_2$SO$_4$), 7.44 (1 s, C$_{14}$H$_2$O$_8$). ^{13}C NMR (126 MHz, DMSO) δ 159.54, 148.30, 139.67, 136.68, 112.70, 110.72, 108.17.

Elemental analyses (C, H, N) were carried out at Robertson Microlit Laboratories in Ledgewood, New Jersey. Measurements were performed in duplicate for DMA-, Na-, K-, Mg-, and TMA-SU-102.

Inductively coupled plasma mass spectrometry (ICP-MS) data was collected at the MIT Center for Environmental Health Sciences (CEHS) using an Agilent 7900 ICP-MS spectrometer. Calibration standards were prepared for ICP-MS analysis using analytical standard solutions purchased from VWR Chemicals BDH Aristar Plus and an aqueous 2% HNO$_3$ solution (prepared from EMD Millipore OmniTrace HNO$_3$ and ultrafiltered water). Digestion of samples was performed in concentrated HNO$_3$ (67-70%, OmniTrace Ultra, EMD Millipore). The cation content (Li, Na, K, Mg) was determined by ratio to Zr content.

Density functional theory (DFT) calculations were performed using the B3LYP functional and def2-TZVP basis set[36] using the Orca computational software[37]. Vibrational Stark tuning rates were calculated by placing two point charges 5 nm from the ketone oxygens and two point charges of opposite charge 30 nm from the ketone oxygens, along the C-O vector.

Thermogravimetric analyses were conducted using a TA Instruments TGA Q5000 using a gas flow rate of 25 mL/min and platinum high-temperature pans. Masses were uncorrected for buoyancy effects. The TGA instrument was connected to air (Airgas, Industrial Grade, Dry) and nitrogen (Airgas, UHP > 99.999%) cylinders. The TGA pans were cleaned using a propane torch. Approximately 5 mg of powder was loaded onto a tared sample pan using a plastic spatula for each measurement.

Scanning electron microscopy (SEM) was conducted using a Zeiss Merlin high resolution scanning electron microscope at MIT MRSEC (formerly the Center for Materials Science and Engineering – CMSE). The samples were mounted on carbon fiber tape before being transferred into the chamber. The images were acquired at a working distance of 4.7–5.0 mm and an electron beam energy of 2.00 kV.

Data availability
The data supporting the findings of the study are included in the main text and supplementary information files. Raw data can be obtained from the corresponding author upon request. Source data are provided with this paper.

References

1. Liu, X., Wang, X. & Kapteijn, F. Water and Metal–Organic Frameworks: From Interaction toward Utilization. *Chem. Rev.* **120**, 8303–8377 (2020).
2. Hanikel, N., Prévot, M. S. & Yaghi, O. M. MOF water harvesters. *Nat. Nanotechnol.* **15**, 348–355 (2020).
3. Zhang, B., Zhu, Z., Wang, X., Liu, X. & Kapteijn, F. Water Adsorption in MOFs: Structures and Applications. *Adv. Func. Mater.* **34**, 2304788 (2024).
4. Shi, L., Kirlikovali, K. O., Chen, Z. & Farha, O. K. Metal-organic frameworks for water vapor adsorption. *Chemistry* (2023) https://doi.org/10.1016/j.chempr.2023.09.005.
5. Oppenheim, J. J. & Dincă, M. Isoreticular Curves: A Theory of Capillary Condensation To Model Water Sorption within Microporous Sorbents. *J. Am. Chem. Soc.* **146**, 20615–20626 (2024).
6. Alezi, D. et al. Tunable Low–Relative Humidity and High–Capacity Water Adsorption in a Bibenzotriazole Metal–Organic Framework. *J. Am. Chem. Soc.* **145**, 25233–25241 (2023).
7. Reinsch, H. et al. Structures, Sorption Characteristics, and Nonlinear Optical Properties of a New Series of Highly Stable Aluminum MOFs. *Chem. Mater.* **25**, 17–26 (2013).
8. Logan, M. W., Adamson, J. D., Le, D. & Uribe-Romo, F. J. Structural Stability of N-Alkyl-Functionalized Titanium Metal–Organic Frameworks in Aqueous and Humid Environments. *ACS Appl Mater. Interfaces* **9**, 44529–44533 (2017).
9. Ko, N. et al. Tailoring the water adsorption properties of MIL-101 metal–organic frameworks by partial functionalization. *J. Mater. Chem. A* **3**, 2057–2064 (2015).
10. Cmarik, G. E., Kim, M., Cohen, S. M. & Walton, K. S. Tuning the Adsorption Properties of UiO-66 via Ligand Functionalization. *Langmuir* **28**, 15606–15613 (2012).
11. Hanikel, N. et al. Evolution of water structures in metal-organic frameworks for improved atmospheric water harvesting. *Science* **374**, 454–459 (2021).
12. Zheng, Z., Hanikel, N., Lyu, H. & Yaghi, O. M. Broadly Tunable Atmospheric Water Harvesting in Multivariate Metal–Organic Frameworks. *J. Am. Chem. Soc.* **144**, 22669–22675 (2022).
13. Liu, J. et al. A Tunable Bimetallic MOF-74 for Adsorption Chiller Applications. *Eur. J. Inorg. Chem.* **2018**, 885–889 (2018).
14. Bon, V., Senkovska, I., Baburin, I. A. & Kaskel, S. Zr- and Hf-Based Metal–Organic Frameworks: Tracking Down the Polymorphism. *Cryst. Growth Des.* **13**, 1231–1237 (2013).
15. Rieth, A. J., Yang, S., Wang, E. N. & Dincă, M. Record atmospheric fresh water capture and heat transfer with a material operating at the water uptake reversibility limit. *ACS Cent. Sci.* **3**, 668–672 (2017).
16. Wright, M. et al. Precise control of pore hydrophilicity enabled by post-synthetic cation exchange in metal–organic frameworks. *Chem. Sci.* **9**, 3856–3859 (2018).
17. Rieth, A. J. et al. Tunable Metal–Organic Frameworks Enable High-Efficiency Cascaded Adsorption Heat Pumps. *J. Am. Chem. Soc.* **140**, 17591–17596 (2018).
18. Rieth, A. J. et al. Record-setting sorbents for reversible water uptake by systematic anion exchanges in metal–organic frameworks. *J. Am. Chem. Soc.* **141**, 13858–13866 (2019).
19. An, H. J., Sarker, M., Yoo, D. K. & Jhung, S. H. Water adsorption/desorption over metal-organic frameworks with ammonium group for possible application in adsorption heat transformation. *Chem. Eng. J.* **373**, 1064–1071 (2019).
20. Svensson Grape, E. et al. Removal of pharmaceutical pollutants from effluent by a plant-based metal–organic framework. *Nat. Water* **1**, 433–442 (2023).
21. Jenkins, H. D. B. & Marcus, Y. Viscosity B-Coefficients of Ions in Solution. *Chem. Rev.* **95**, 2695–2724 (1995).
22. González-Jiménez, M., Liao, Z., Williams, E. L. & Wynne, K. Lifting Hofmeister's Curse: Impact of Cations on Diffusion, Hydrogen Bonding, and Clustering of Water. *J. Am. Chem. Soc.* **146**, 368–376 (2024).
23. Evans, R., Marconi, U. M. B. & Tarazona, P. Fluids in narrow pores: Adsorption, capillary condensation, and critical points. *J. Chem. Phys.* **84**, 2376–2399 (1986).
24. Rieth, A. J., Hunter, K. M., Dincă, M. & Paesani, F. Hydrogen bonding structure of confined water templated by a metal-organic framework with open metal sites. *Nat. Commun.* **10**, 4771 (2019).

25. Shimizu, S. & Matubayasi, N. Temperature Dependence of Sorption. *Langmuir* **37**, 11008–11017 (2021).

26. Water - Heat of Vaporization vs. Temperature. https://www.engineeringtoolbox.com/water-properties-d_1573.html.

27. Bezrukov, A. A. et al. Metal-organic frameworks as regeneration optimized sorbents for atmospheric water harvesting. *Cell Rep. Phys. Sci.* **4**, 101252 (2023).

28. Dalla Bernardina, S. et al. Water in Carbon Nanotubes: The Peculiar Hydrogen Bond Network Revealed by Infrared Spectroscopy. *J. Am. Chem. Soc.* **138**, 10437–10443 (2016).

29. Bregante, D. T. et al. The shape of water in zeolites and its impact on epoxidation catalysis. *Nat. Catal.* **4**, 797–808 (2021).

30. Di Iorio, J. R., Johnson, B. A. & Román-Leshkov, Y. Ordered Hydrogen-Bonded Alcohol Networks Confined in Lewis Acid Zeolites Accelerate Transfer Hydrogenation Turnover Rates. *J. Am. Chem. Soc.* **142**, 19379–19392 (2020).

31. Fried, S. D. & Boxer, S. G. Electric Fields and Enzyme Catalysis. *Annu Rev. Biochem* **86**, 387–415 (2017).

32. Fried, S. D., Bagchi, S. & Boxer, S. G. Extreme electric fields power catalysis in the active site of ketosteroid isomerase. *Science* **346**, 1510–1514 (2014).

33. Bagchi, S., Fried, S. D. & Boxer, S. G. A Solvatochromic Model Calibrates Nitriles' Vibrational Frequencies to Electrostatic Fields. *J. Am. Chem. Soc.* **134**, 10373–10376 (2012).

34. Bhattacharyya, D. et al. Vibrational Stark shift spectroscopy of catalysts under the influence of electric fields at electrode–solution interfaces. *Chem. Sci.* **12**, 10131–10149 (2021).

35. Hofmeister, F. Zur Lehre von der Wirkung der Salze. *Arch. f. Exp. Pathol. u. Pharmakol.* **24**, 247–260 (1888).

36. Weigend, F. & Ahlrichs, R. Balanced basis sets of split valence, triple zeta valence and quadruple zeta valence quality for H to Rn: Design and assessment of accuracy. *Phys. Chem. Chem. Phys.* **7**, 3297–3305 (2005).

37. Neese, F., Wennmohs, F., Becker, U. & Riplinger, C. The ORCA quantum chemistry program package. *J. Chem. Phys.* **152**, 224108 (2020).

38. Reinsch, H. et al. A new Al-MOF based on a unique column-shaped inorganic building unit exhibiting strongly hydrophilic sorption behaviour. *Chem. Commun.* **48**, 9486–9488 (2012).

39. Cho, K. H. et al. Hydrothermal Green Synthesis of a Robust Al Metal-Organic-Framework Effective for Water Adsorption Heat Allocations. *ACS Sustain Chem. Eng.* **10**, 7010–7019 (2022).

40. Cadiau, A. et al. Design of Hydrophilic Metal Organic Framework Water Adsorbents for Heat Reallocation. *Adv. Mater.* **27**, 4775–4780 (2015).

41. Zheng, Z., Alawadhi, A. H. & Yaghi, O. M. Green Synthesis and Scale-Up of MOFs for Water Harvesting from Air. *Mol. Front J.* **07**, 20–39 (2023).

42. Furukawa, H. et al. Water Adsorption in Porous Metal–Organic Frameworks and Related Materials. *J. Am. Chem. Soc.* **136**, 4369–4381 (2014).

Competing interests
The authors declare no competing interests.

Additional information
Supplementary information The online version contains supplementary material available at https://doi.org/10.1038/s41467-025-59551-2.

Correspondence and requests for materials should be addressed to Mircea Dincă.

Peer review information *Nature Communications* thanks Dalal Alezi, Sachin Chavan and the other, anonymous, reviewer(s) for their contribution to the peer review of this work. A peer review file is available.

Reprints and permissions information is available at http://www.nature.com/reprints

Publisher's note Springer Nature remains neutral with regard to jurisdictional claims in published maps and institutional affiliations.